

# Effect of Annealing Time on Microstructure Stability and Mechanical Behavior of Ferrite-Cementite Steel with Multiscale Lamellar Structure



DONGMEI ZHANG, MINGHE ZHANG, KUO CAO, JIANGLI NING,  
and YUNLI FENG

Plain medium carbon steel with multiscale ferrite ( $\alpha$ ) + cementite ( $\theta$ ) lamellar structure was produced by warm rolling and subsequently annealing. The effect of annealing time on microstructural evolution was studied via scanning electron microscope and electron backscatter diffraction. The obtained results showed that the feature of multiscale lamellar microstructure remained virtually the same with annealing times from 10 to 60 minutes, while the increase of annealing time destabilizes the stability of the microstructure. The specimen annealed for 30 minutes demonstrated good combination of strength and ductility because of the improvement of strain strengthening ability. The strain hardening behavior was described by instantaneous strain hardening exponent ( $n_i$ ) and modified Crussard–Jaouli (C–J) model. Furthermore, the respective strengthening contribution of grain refinement, sub-grain strengthening and cementite particles to the yield strength was investigated in detail.

<https://doi.org/10.1007/s11663-021-02075-z>

© The Minerals, Metals & Materials Society and ASM International 2021

## I. INTRODUCTION

PLAIN medium carbon steels are commonly used in bridge construction and mechanical design fields due to their good combination of strength and ductility.<sup>[1,2]</sup> In order to further improve the comprehensive mechanical properties of medium carbon steel, the traditional method were refining the grain to obtain ultrafine grained structure or add a variety of alloy elements.<sup>[3,4]</sup> Regarding the economy, Lu<sup>[5]</sup> put forward the concept of “Making Materials Plain”, that is, with less alloying or even non-alloying are added to achieve a durable plastic synergistic effect. When the grain size is lower than 1  $\mu\text{m}$ , although the strength is significantly enhanced, the plastic is usually sacrificed due to the weak strain hardening ability.<sup>[6]</sup> According to the Considère criterion, a high rate of strain hardening can effectively avoid local strain instability, achieve stable and uniform tensile deformation before the occurrence of necking, and improve the uniform

elongation. Therefore, to improve the synergy of strength and ductility of fine-grained materials, it is necessary to improve their strain hardening capability.

Tremendous efforts have been paid to evade strength and ductility trade-off of metallic materials. Approaches such as the ultrafine structure with nano-twins<sup>[7]</sup>; mixed crystal structure composed of nano- and micron-scale grains<sup>[8]</sup>; transformation-induced plasticity (TRIP) effect<sup>[9–11]</sup>; ultrafine structure with distribution of hard phase<sup>[12]</sup>; and gradient structure of nano-to micron-scale grains<sup>[13–15]</sup> can improve the comprehensive mechanical properties of structural materials. Moreover, a number of experiments showed that the bimodal distribution, one of the hetero-structures of plain carbon steels, remarkable enhance the strain hardening capability. Zheng *et al.*<sup>[16]</sup> designed a eutectoid steel with equiaxed-ferrite grains and bimodal cementite grains distribution structure via warm deformation and annealing. The results show that the bimodal structure displays higher strength than ultrafine eutectoid steel structure which with a single size. The grain size rang micrometers to millimeters can exhibit decent uniform elongation.<sup>[17,18]</sup> For example, the soft coarse grained lamellar domains embedded in hard ultrafine grained matrix,<sup>[17]</sup> which has unprecedented uniform elongation because the high strain partition between soft and hard domains during deformation.

---

DONGMEI ZHANG, MINGHE ZHANG, KUO CAO, JIANGLI NING, and YUNLI FENG are with the College of Metallurgy and Energy, North China University of Science and Technology, Tangshan, 063210, Hebei, China. Contact e-mail: tsfengyl@163.com

Manuscript submitted September 19, 2020; accepted January 8, 2021.

Article published online February 23, 2021.

It has been recognized that the lamellar structure could be regarded as a kind of method to alleviate ductility degeneration without loss much strength in ultrafine-grained structure.<sup>[19,20]</sup> Sun *et al.* found that by introducing the lamellar structure of low carbon steel plate can produce an extra strengthening, and exhibit higher lower-shelf energy and lower ductile-to-brittle transition temperature compare with the coarse grains steel. In addition, Huang *et al.*<sup>[21]</sup> showed that via introducing the layered composite of Ti-Al, strain delocalization was effectively relieved by the strain partition between Ti and Al lamellar and thus achieved the good combination of strength and ductility.

Inspired by the researches of lamellar and hetero-structures to optimize the properties, in this report, medium carbon steel with a dual-phase multi-scale ( $\alpha + \theta$ ) lamellar structure was obtained via thermo-mechanical processing, *i.e.*, warm rolling of pseudo-eutectoid microstructure (the pseudo-eutectoid microstructure was produced by pre-treatment of medium carbon steel) and subsequent annealing. Effect of annealing time on the microstructure evolution and mechanical properties was investigated. In addition, based on the roles of the ferrite matrix and cementite particles in the process of strain hardening, the contributions of different strengthening mechanisms to the yield strength of the specimen are discussed in detail.

## II. MATERIALS AND EXPERIMENTAL PROCEDURE

The material used was a plain medium-carbon steel with the chemical composition (wt pct) 0.45 C, 0.54 Mn, 0.26 Si, 0.019 S, and 0.021 P. Microstructure of plain medium-carbon steel as shown in Figure 1(a). The as-received bar was machined into 15 mm  $\times$  15 mm  $\times$  150 mm rectangular specimens for subsequent pre-treat and warm rolling. The specimens were heated to and maintained at 870 °C for 45 minutes and were quenched in hot-water at 90 °C with a cooling rate of about 24 °C/s. Under the low cooling rate, a pseudo-eutectoid microstructure was obtained, as shown in Figure 1(b).

The quenched specimens were reheated to 550 °C for 15 minutes and rolled for 8 passes. Rolling reduction was set at  $\sim$  20 pct per pass. The final steel plate thickness was 2.4 mm. The total reduction ratio was 84 pct and the accumulated strain was 1.8. The specimens were annealing temperature at 600 °C for 10, 15, 30 and 60 minutes, respectively. The microstructures were characterized with FEI Quanta-650 FEG field emission scanning electron microscope (SEM). The specimens were cut on the strip specimens with different annealing time and prepared by corrosion in 4 pct alcohol nitrate solution after mechanical polishing. The grain size and distribution was characterized by electron backscatter diffraction (EBSD). Annealed specimens were scanned with a step size of 90nm. The electrolytic polishing solution was composed of 80 pct C<sub>2</sub>H<sub>5</sub>OH + 15 pct HClO<sub>4</sub> and 5 pct glycerol. The electrolytic voltage was 28V and the current was 0.1 A. Image-Pro Plus 6.0 image analysis software was used to measure the average cementite distance and other structural parameters of the annealed steel. The tensile test at room temperature was conducted by Instron electronic universal test machine under the strain rate of  $5 \times 10^{-4} \text{s}^{-1}$ . The tensile samples (dog bone shaped) were cut from annealed plates along the rolling direction with a thickness of 1.0 and 3 mm width, 15 mm length.

## III. RESULTS

### A. Microstructure

Figure 1 shows the SEM images of medium carbon steel after pre-treatment and warm rolling. The initial structure of plain medium carbon steel is shown in Figure 1(a), with ferrite and pearlite structure, among which the proportion of pro-eutectoid ferrite is 42.7 pct. After austenitizing and water quenching, the structure was transformed into a pseudo-eutectoid structure of pro-eutectoid ferrite + pearlite group, as shown in Figure 1(b). The pro-eutectoid ferrite accounted for 14 pct, significantly less than that of the initial specimen. As shown in Figure 1(c), after the warm rolling, the specimen obviously presents a dual-phase ( $\alpha + \theta$ )

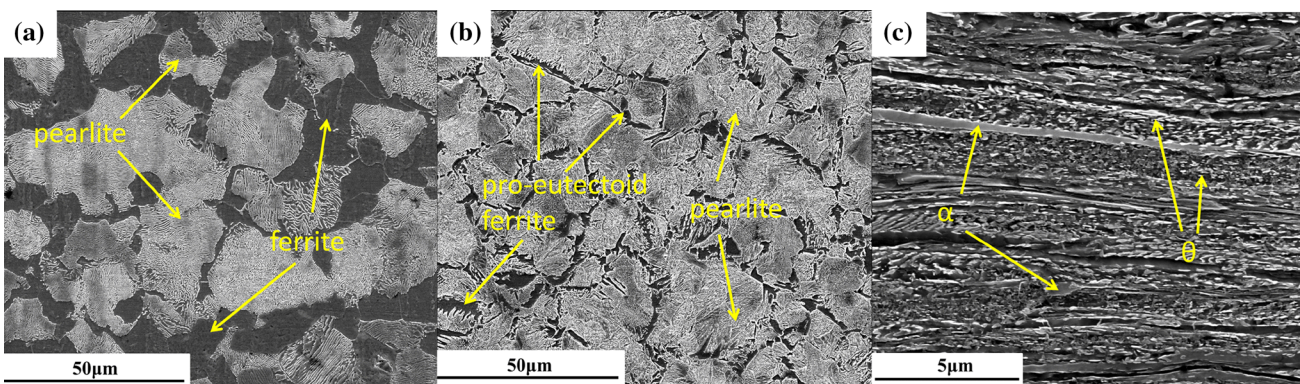


Fig. 1—SEM image of (a) initial and (b) quenched state of medium carbon steel; (c) Microstructure of quenched specimen after warm rolling.

heterogeneous lamellar structure, and the ferrite is elongated into lamellar with different thickness along the rolling direction. The cementite lamellae are fractured and distributed particles or short rods in intergranular and intragranular, there is no obvious diffusion of carbon atoms.

Figures 2(a) through (d) show the SEM images of samples annealed at 600 °C for different times after warm rolling. When annealing for 10 minutes (Figure 2(a)), most of the cementite was spherical and the original pearlite lamellar completely disappeared; some of the eutectoid ferrite grains were recrystallized. Because the ferrite grains boundaries in the original pearlite area were pinned by cementite, the grain size after recrystallization is small. When annealing for 15 minutes (Figure 2(b)), ferrite grains begin to grow. There are more spheroidized cementite particles inside the ferrite grains. However, there are still some banded ferrite structures that only recover but not recrystallize, forming fine sub-grains. As shown in Figure 2(c), when

annealing for 30 minutes, a small amount of pro-eutectoid ferrite disappeared, the grain size of ferrite was slightly larger than that of sample annealing for 15 minutes, and coarse cementite at the grain boundary was observed. This is because a high concentration of dislocations or vacancies is generated after warm rolling, which helps carbon atoms diffuse to a region with low carbon concentration (pro-eutectoid ferrite), and then precipitation at the most favorable position of energy (trigeminal grain boundary of ferrite grain boundary).<sup>[22,23]</sup> Due to the high diffusion rate at the grain boundary, the particles located at the trigeminal grain boundary have a size advantage during the post-annealing process. When annealing for 60 minutes (Figure 2(d)), most of the deformed ferrite recrystallized, and some recrystallized ferrite grains have begun to grow, and the ferrite is arranged in the rolling direction. The cementite is further coarsened than that of sample annealing for 30 minutes. The average grain size of ferrite is 0.138  $\mu\text{m}$ , a few grains up to 0.300  $\mu\text{m}$  exist.

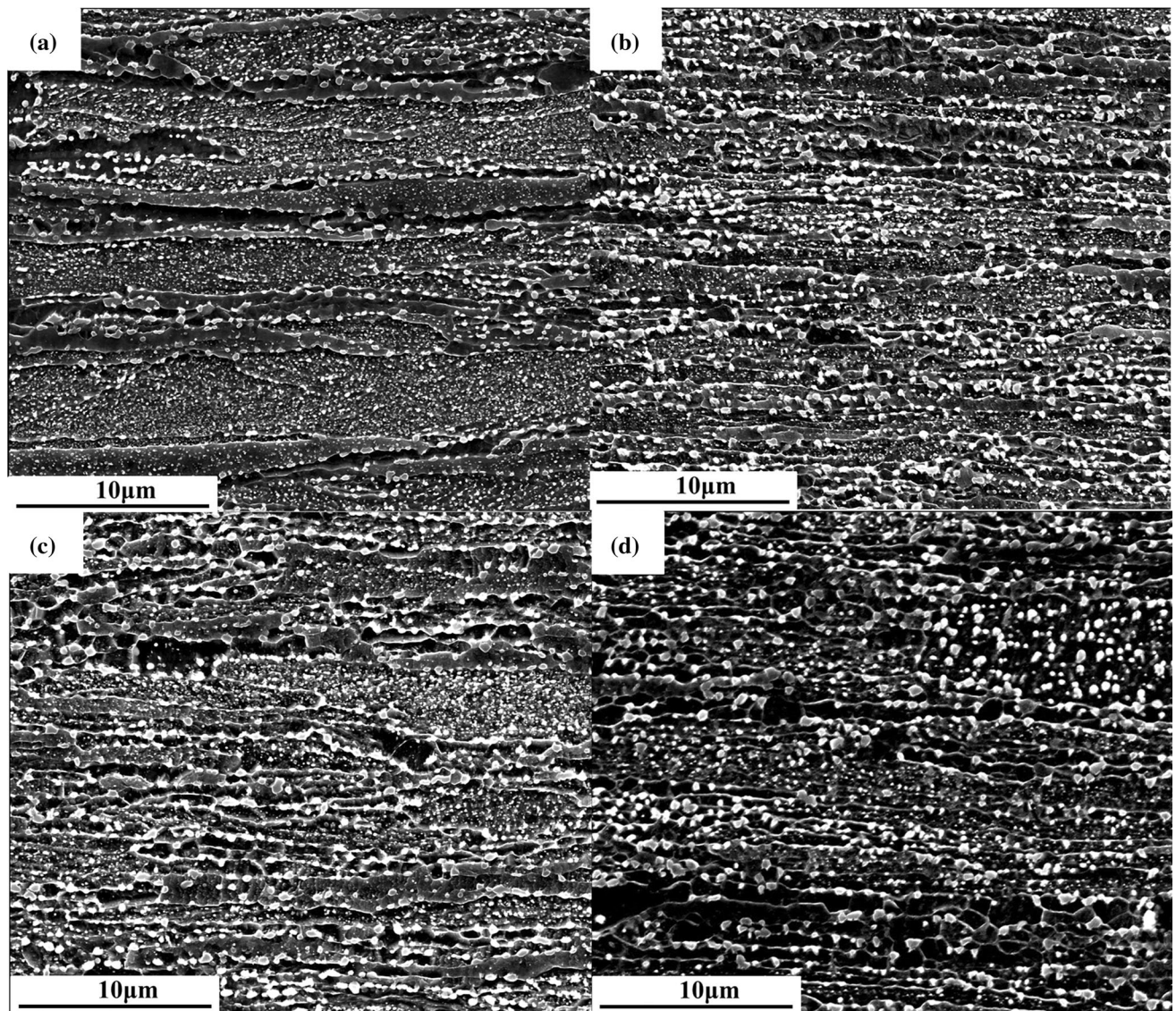


Fig. 2—The SEM micrograph of the specimen annealing for (a) 10 min; (b) 15 min; (c) 30 min; (d) 60 min.

The orientation distribution of annealing specimens obtained by EBSD maps are shown in Figure 3, in which the proportion of high/low angle grain boundaries and grain sizes are counted. The grain size of ferrite matrix is multiscale distribution (Figure 4). The reason of multiscale distribution is that the original pearlite area in the presence of large amounts of cementite after warm rolling, it leads to the movement of grain boundary blocked, so the grain growth rate of the region in the process of annealing is more slower and form the finer ferrite grain. While the pro-eutectoid ferrite area due to the small number of cementite, by the grain boundary barrier is lesser, form a larger ferrite grain in the process of annealing.<sup>[22,24]</sup>

When the annealing time is 10, 15, 30, 60 minutes, the corresponding average sub-grain size is 0.59, 0.63, 0.68 and 0.75  $\mu\text{m}$  and the average size of cementite particles is 0.115, 0.121, 0.129, 0.138  $\mu\text{m}$  (Figure 5). The average grain sizes confirmed in this way could elucidate the relationship between grain size and yield strength as mentioned later in 4.3. With the annealing time increasing, the proportion of small grains gradually decreases while the proportion of large grains increases. In this work, the microstructural parameters which considered play an important role in the discussion of yield strength are summarized in Table I.

## B. Mechanical Properties

Figure 6 shows the engineering stress-strain curves of multiscale ( $\alpha + \theta$ ) structure at different annealing times. The detailed mechanical properties are outlined in Table II. The specimen annealing at different times showed the characteristics of discontinuous yielding.

The Lüders strain corresponding to 10, 15, 30, and 60 minutes were 0.4, 0.68, 1.6 and 1.4 pct, respectively. During the hetero-uniform deformation, the hard cementite particle is seen as a barrier to dislocations through ferrite grains and lead to the increase of Lüders strain.<sup>[25,26]</sup> The specimen annealed for 10 minutes exhibits a yield strength ( $\sigma_b$ ) and a tensile strength ( $\sigma_s$ ) of 708 and 790 MPa, respectively, in addition to a uniform elongation of 6.3 pct and total elongation is 8.4 pct. By extending the annealing time to 60 minutes, the uniform elongation and total elongation increase to 8.6 and 11.6 pct, but strength is sacrificed and decrease 53 MPa of  $\sigma_b$  and 60 MPa of  $\sigma_s$ . There are two main reasons for this phenomenon: on the one hand, the long-time annealing increases the degree of ferrite grain coarsening. According to the Hall–Petch relationship, the increase in grain size will inevitably lead to a decrease in strength and ferrite softening. On the other hand, with the extension of annealing time, the stability of the structure decreases, and the multiscale distribution of ferrite gradually becomes weaker after recrystallization (the distribution of ferrite grain size shown in Figure 4).

By comparing the mechanical properties of the experimental steel at different annealing times (Table II), it can be concluded that the toughness at 30 minutes of annealing to 5600 MPa · pct and exhibits a longer stable deformation stage, which is attributed to the increase of strain hardening ability. The multiscale lamellar structure causes strain gradient effect and multi-axial stress state during tensile deformation resulting in the effective accumulation of geometric necessary dislocations (GND), leading to the effective improvement of the strain strengthening ability.<sup>[17,18]</sup> This also

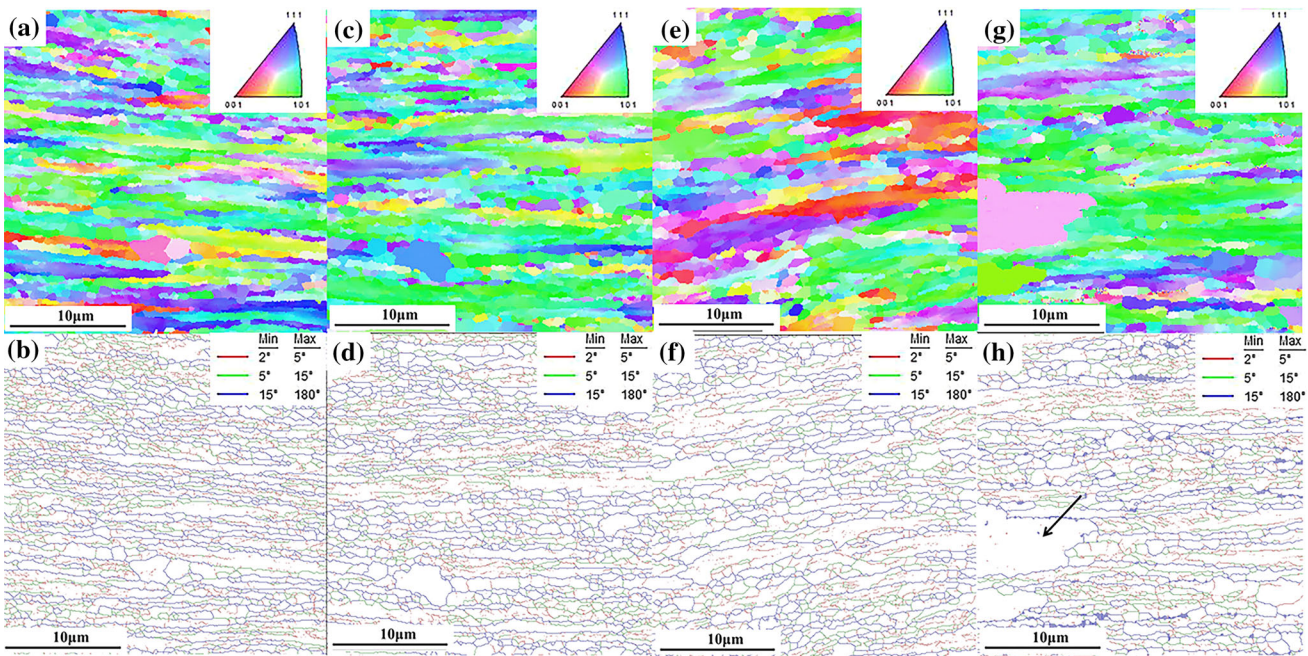


Fig. 3—The EBSD and the boundary map of dual-phase multiscale ( $\alpha + \theta$ ) lamellar structure annealed for (a) and (b) 10 min; (c) and (d) 15 min; (e) and (f) 30 min; (g) and (h) 60 min, wherein the blue, green and red lines denote the misoriented at  $\geq 15^\circ$ ,  $5^\circ \leq \theta \leq 15^\circ$  and  $2^\circ \leq \theta \leq 5^\circ$ , respectively. (For interpretation of the references to color in this figure legend, the reader is referred to the web version of this article.)

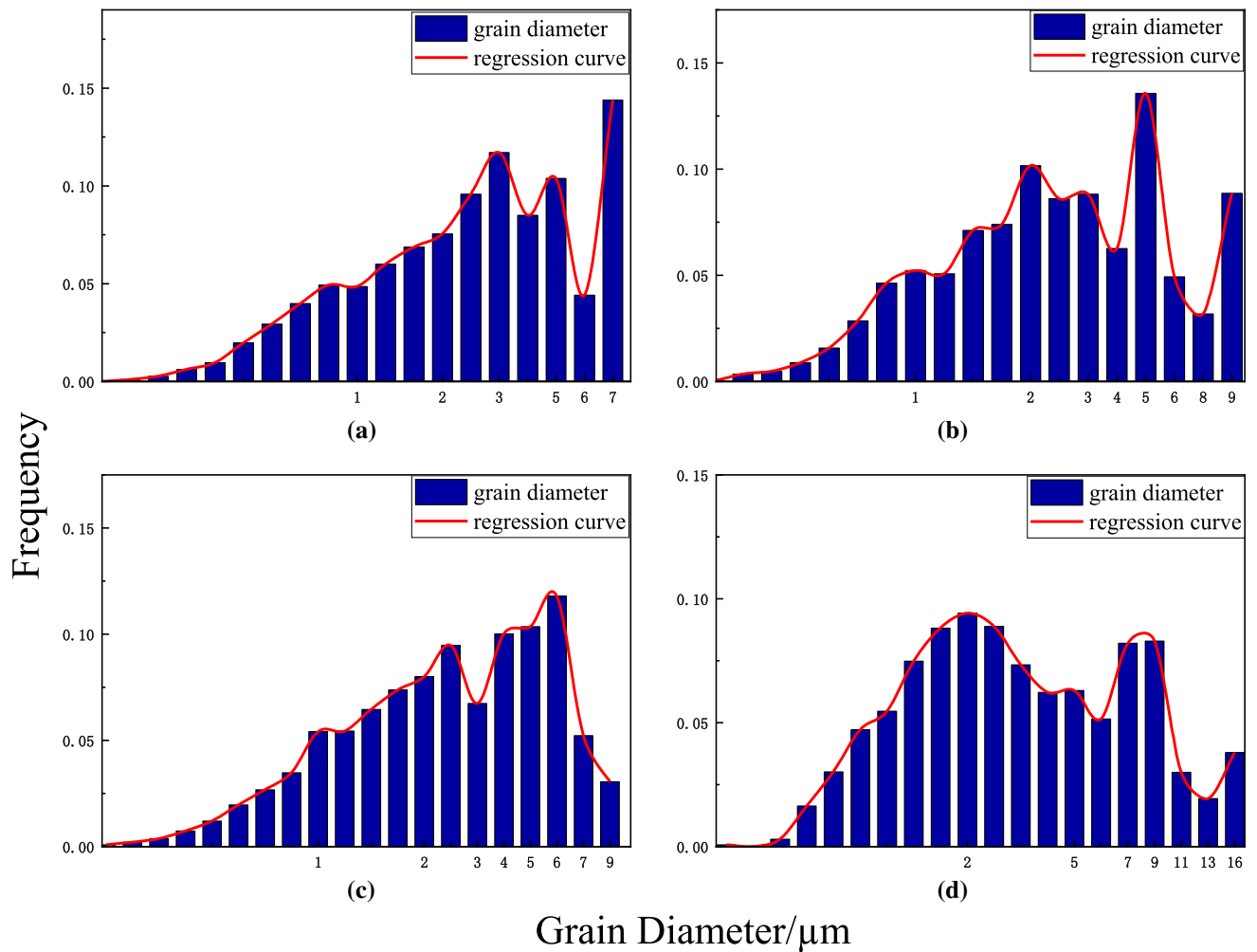


Fig. 4—The size distributions of ferrite grain at different time of annealing at 600 °C for different times (a) 10 min; (b) 15 min; (c) 30 min; (d) 60 min.

shows that the structure of the multiscale lamellar ( $\alpha + \theta$ ) obtained during annealing for 30 minutes can achieve the optimal combination of strength and plasticity.

#### IV. DISCUSSION

##### A. The Stability of Annealed Structure

Materials with homogeneous nano-grain structure are thermally unstable compared with the regular coarse grains structure and show a greater tendency to go through grain coarsening. In the following, the thermal stability of multiscale ( $\alpha + \theta$ ) lamellar structure steel will be discussed. It can be observed from Figure 3, as the annealing time increased, the band-shaped pro-eutectoid ferrite in the structure becomes wider, and the eutectoid ferrite in the original pearlite field is still relatively small, the growth is not obvious. Combined with the SEM image of Figure 2, it can be concluded that the ferrite in the original pearlite is pinned by cementite, and its softening tendency (cause by recrystallization form new grains) is lower than that of pro-eutectoid ferrite. Ferrite

coarsening is especially obvious after annealing for 60 minutes, which proves that one of the reasons for the decrease in yield strength is the softening of ferrite. The experiment confirmed the conjecture proposed by the literature<sup>[23,27]</sup>: in the multi-scale layered structure, the structure with a smaller ferrite/spheroid cementite interface is more stable than the structure with a larger ferrite/cementite interface.

It is worth noting that the abnormally large grains shown by the arrows in Figure 3(h) is mainly due to the local energy storage gradient caused by the warm rolling process, which helps the preferential growth of a few grains with high angle grain boundaries; some pro-eutectoid ferrite grain boundaries have fewer cementite particles, which lacks the pinning effect of cementite particles during their growth. This also confirms the conclusion that the stability of the ferrite in the original pearlite is better than the pro-eutectoid ferrite. And, more remarkable, combining Figures 3 and 4, the initial pseudo-eutectoid structure carbon steel was designed and fabricated by annealing at different times after warm rolling, the ferrite grains after recrystallization still maintain a multiscale distribution, but with the

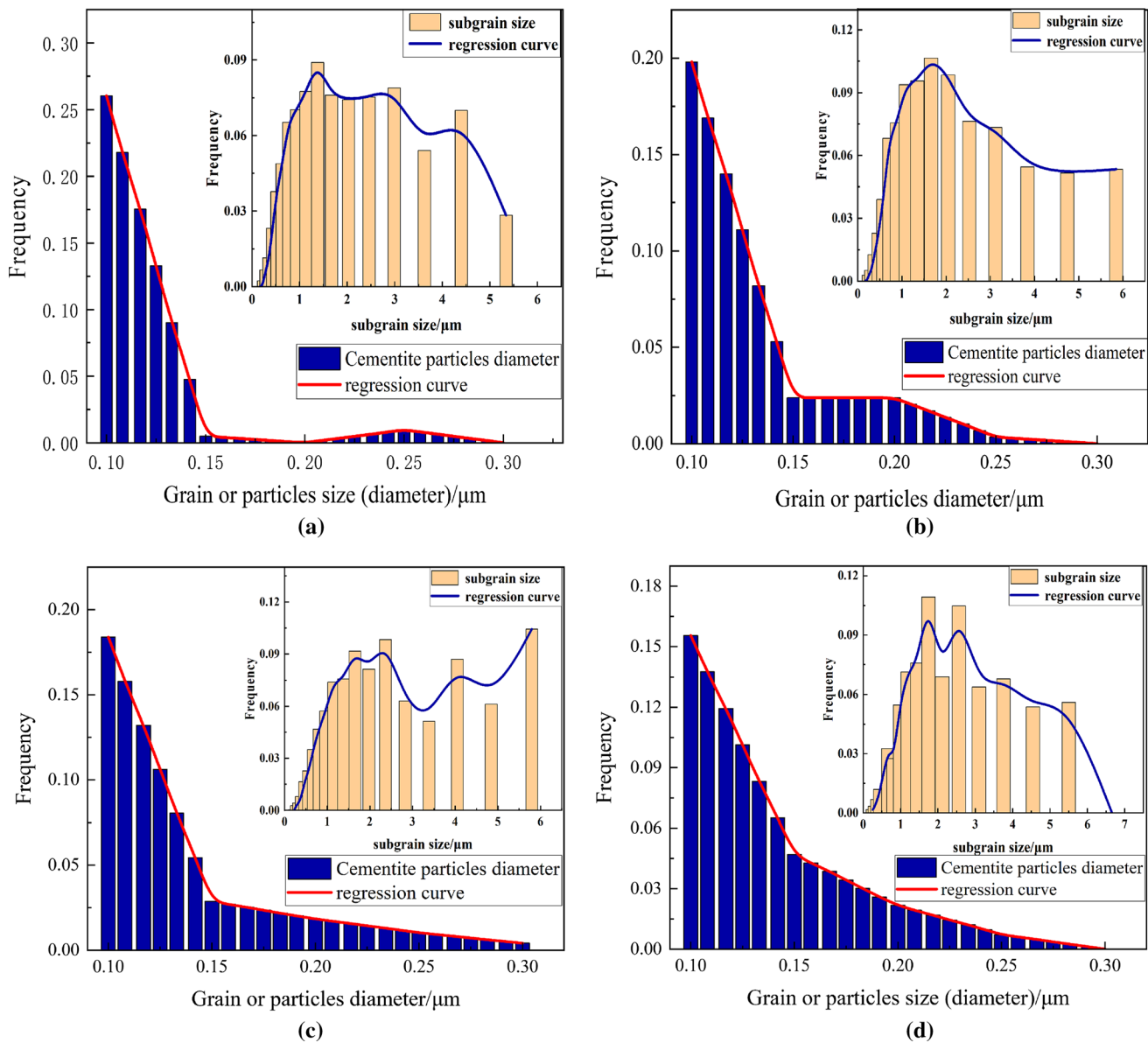


Fig. 5—The grain diameter distribution of sub-grain and cementite particles at different annealing times (a) 10 min; (b) 15 min; (c) 30 min; (d) 60 min.

increase of annealing time, this multi-scale distribution phenomenon gradually weakens. When annealed for 60 minutes, the multi-scale layered structure weakened significantly.

Figure 4 shows the ferrite grain size distribution at different annealing times. When the annealing time is 10, 15, 30, 60 minutes, the ferrite grains of the corresponding specimen all have multiscale distribution characteristics. It can be observed that with the increase of the annealing time, the recovery and recrystallization process take place in the ferrite grains, and the large grains continue to grow, but due to the Zener pinning of the grain boundaries by the spheroidizing precipitation of

cementite,<sup>[23]</sup> the migration of high angle grain boundaries is hindered, so that the average grain size at different times during annealing is not much different.

Figure 7 is the distribution of orientation differences of specimens at different annealing times at 600 °C. When the annealing time is 10, 15, 30, 60 minutes, the corresponding proportions of the specimen's low angle grain boundaries is 52.5, 51.3, 50.1, and 42.8 pct, respectively. When annealing for 10 to 30 minutes, the proportion of low angle grain boundaries is not much different, but when the annealing time increased to 60 minutes, the proportion of low angle grain boundaries decreases sharply. This is mainly caused by the following

**Table I. Experimental Statistics of the Parameters of Each Yield Strength**

Annealing time/min	$(\theta)_{\text{LAB}}/^\circ$	$d_{\text{SG}}/\mu\text{m}$	$d/\mu\text{m}$	$d_p/\mu\text{m}$	$L/\mu\text{m}$
10	6.15	0.59	0.98	0.115	0.61
15	6.12	0.63	1.05	0.121	0.55
30	5.97	0.68	1.15	0.129	0.49
60	5.93	0.75	1.32	0.138	0.40

$(\theta)_{\text{LAB}}$  is the mean orientation of low angle grain boundary;  $d_{\text{SG}}$  is the average sub-grain diameter;  $d$  is the average grain size of ferrite;  $d_p$  is the average grain size of cementite;  $L$  is the average distance of cementite particles.

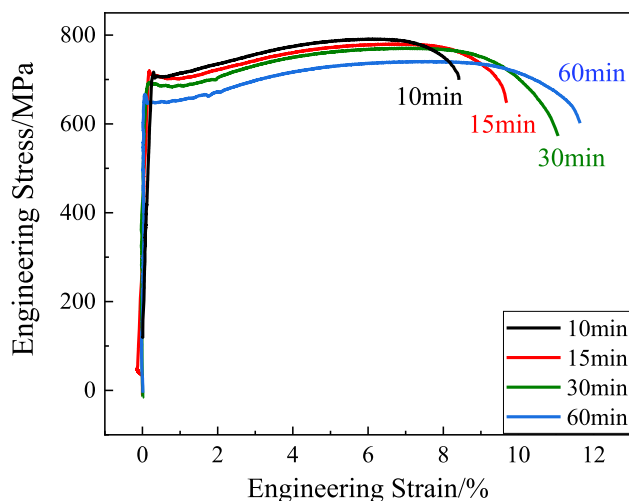


Fig. 6—The Engineering stress-strain curves for the annealed specimens with multiscale ( $\alpha + \theta$ ) structure.

**Table II. Mechanical Properties of the Multiscale ( $\alpha + \theta$ ) Lamellar Structure**

Annealed time/min	$\sigma_b$ (MPa)	$\sigma_s$ (MPa)	$\delta_u$ (pct)	$\delta_t$ (pct)	Toughness (MPa·pct)
10	790	708	6.3	8.4	4460
15	778	701	7.3	9.6	5117
30	768	683	8.2	11.0	5600
60	737	648	8.6	11.6	5572

$\delta_u$  is the engineering uniform elongation;  $\delta_t$  is the engineering total elongation and the toughness is calculation by  $\sigma_s$  multiply  $\delta_u$ .

reasons: Firstly, the increase of the annealing time promotes the spheroidization and uniform distribution of cementite (as shown in Figure 2), hindering the formation of high angle grain boundaries and the migration of boundaries. Secondly, the dislocations inside the ferrite grains can have enough time to move due to the increase of the annealing time. The dislocations merge and annihilate, so that part of the unit cell substructure formed by severe deformation gradually disappears, and some sub-grain boundaries continuously absorbing the dislocations in the grains, increasing the thickness of the sub-grain boundaries, resulting in a larger orientation difference between the sub-grains, and thus the proportion of the low-angle grain boundaries decreases.

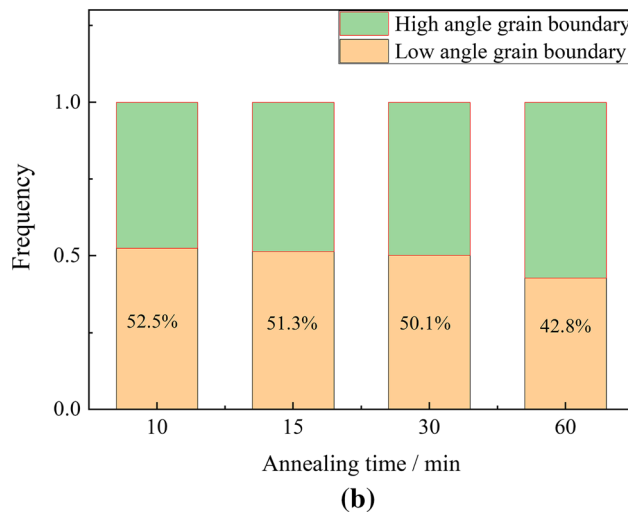
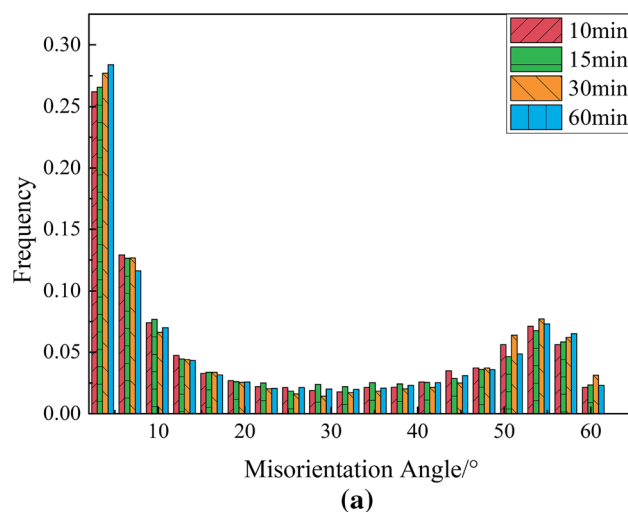


Fig. 7—(a) The distribution of orientation difference at different annealing times at 600 °C and (b) the proportion of high/low angle grain boundaries at different annealing times at 600 °C.

Some researchers found that the energy stored in the form of dislocations and grain boundaries provides the driving force for the recrystallization and coarsening of deformed nanostructure grains.<sup>[28,29]</sup> Therefore, reducing the excess energy at the interface and obtaining grain boundaries with high thermal stability and low mobility can stabilize the metal nanostructures and make them more resistant to annealing. In the dual-phase multiscale medium carbon steel, the low angle grain boundary can effectively stabilize the microstructure, so the

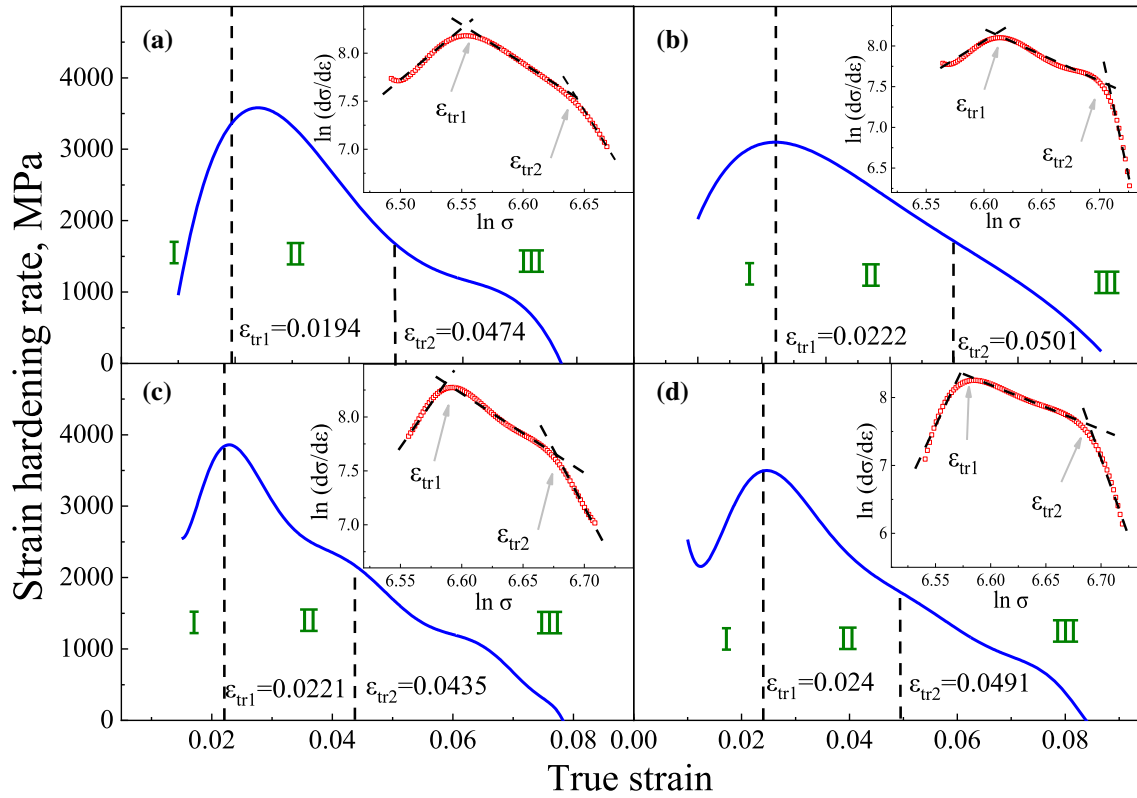


Fig. 8—The strain hardening curve and modified C–J analysis curves (embedded figure) of annealed specimens for (a) 10 min; (b) 15 min; (c) 30 min; (d) 60 min.

microstructure is stable within 30 minutes, and the annealing stability of structure characteristics drops significantly for 60 minutes.

### B. Strain-Hardening Behavior

The strain-hardening behavior of dual phase (DP) steel was usually analyzed based on Hollomon,<sup>[30]</sup> Ashby,<sup>[31]</sup> Kocks-Mecking model<sup>[32]</sup> and Crussard–Jaoul model.<sup>[33]</sup> What should be mentioned is that the application of these analyses varies according to the materials. S.A. Eteami *et al.*<sup>[34]</sup> reported that the modified Crussard–Jaoul (C–J) model can reflect the three stages of strain hardening behavior in ferrite-martensite DP steel. In this part, the strain hardening behavior of the annealed specimen was studied in terms of the instantaneous strain hardening exponent ( $n_i$ ), and the modified C–J model.

The modified C–J model can characterize the stage of strain hardening behavior of the studied materials. The true stress-strain curves of the experimental steels can be analyzed according to the Swift theory<sup>[35]</sup>:

$$\varepsilon = \varepsilon_0 + C\sigma^m \quad [1]$$

Herein,  $C$  is a constant of the studied material,  $m$  is strain hardening exponent of modified C–J model,  $\varepsilon_0$  is the initial true strain. The critical strain is obtained by the change in the slopes of  $\ln \frac{d\sigma}{d\varepsilon}$  as a function of true stress-strain, to analyze the variation of

the strain-hardening process. The modified C–J model uses the logarithmic derivative of the stress-strain relationship as a function of true strain, and derives Eq. [2].

$$\ln \frac{d\sigma}{d\varepsilon} = (1 - m) \ln \sigma - \ln Cm \quad [2]$$

The strain-hardening rate curves of the multiscale ( $\alpha + \theta$ ) lamellar structure steel under different conditions of annealing progress as illustrated in Figure 8, the  $\ln \frac{d\sigma}{d\varepsilon}$  vs.  $\ln \sigma$  plots (that are superimposed in Figure 8) are presented. The sharp change of the slope indicates the change of the plastic deformation mechanism, so the value of critical strain between deformation stages are defined as the transition strain ( $\varepsilon_{tr}$ ) to dividing the strain hardening curve to three stages.

The stage I with true strain about 0.019 to 0.022 is related to the evolution of GND, the dislocation sources in ferrite grains produce multiple mobile dislocations. The dislocations interact with grain boundaries and cementite particles, lead to strain hardening rate and  $n_i$  (Figure 9) rise to adapt the strain gradient caused by the multiscale ferrite distribution. In stage II with true strain about 0.043 to 0.050, almost all specimens reach the max strain hardening rate with true strain at  $\varepsilon_{tr1}$ . Then the curve drops, the reason of it is strain hardening behavior can be understood as the result of dynamic balance between two aspects: dislocation accumulation and dynamic recovery,<sup>[8]</sup> the dynamic recovery becomes dominant in recrystallized grains during the tensile



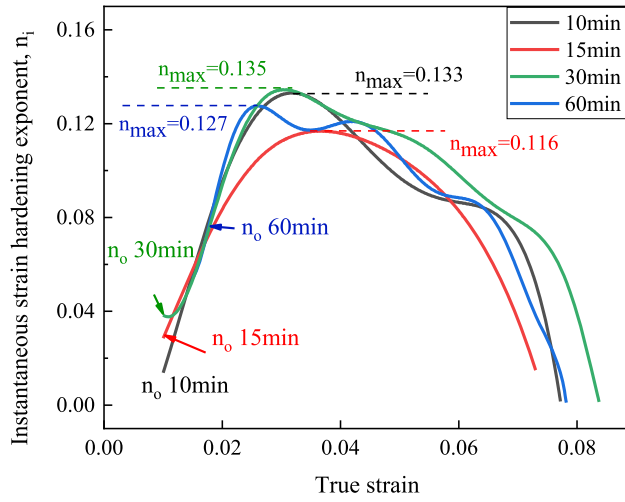


Fig. 9—The instantaneous strain hardening exponent of the annealed specimens with multiscale ( $\alpha + \theta$ ) structure.

strain stage II. In this stage, the  $\alpha$  matrix deforms plastically but  $\theta$  remains elastic. In stage III, the decrease of strain hardening rate to necking is attributed to the occurrence of plastic deformation in both  $\alpha$  and  $\theta$ .

The Hollomon equation can represent the flow stress of materials as follows:

$$\sigma = k\varepsilon^n \quad [3]$$

where  $\sigma$  is true stress,  $\varepsilon$  is true strain and  $k$  is a strength coefficient related to materials. Taking the logarithm of the Hollomon equation yields Eq. [4],

$$\ln \sigma = \ln k + n \ln \varepsilon \quad [4]$$

The instantaneous strain hardening exponent ( $n_i$ ) can be obtained by Eq. [5]:

$$n_i = \frac{d \ln \sigma}{d \ln \varepsilon} \Big|_i = \frac{\varepsilon}{\sigma} \frac{d \sigma}{d \varepsilon} \Big|_i = \frac{\varepsilon_i (\sigma_{i+1} - \sigma_{i-1})}{\sigma_i (\varepsilon_{i+1} - \varepsilon_{i-1})} \quad [5]$$

The plots of  $n_i$  corresponding to specimens annealed for different times are presented in Figure 9. At the initial stage of strain, the value of  $n_0$  is related to the elastoplastic behavior and Lüders strain of materials. It is evident that after a constant initial value ( $n_0$ ), the  $n$  value of all annealed specimens gradually increased to the maximum value ( $n_{max}$ ) and  $n_{max}$  appears approximately in the middle stage of plastic strain. From  $n_0$  to  $n_{max}$ , the accumulation and interaction of dislocations generated leads to specimen exhibits an increase strain hardening rate. The specimen annealed 30 minutes show the highest value of  $n_{max}$  which agree well with the highest strain hardening rate in Figure 8(c), represents the most durable strain hardening. This phenomenon can be attributed to the strain gradient due to mechanical incompatibility in Poisson's ratio between coarse grains ( $\nu \approx 0.5$ ) and ultrafine grains ( $\nu \approx 0.3$ ).<sup>[36,37]</sup> In order to adapt to the strain gradient during plastic deformation, GND will accumulate throughout the microstructure, which will improve the strain hardening ability and thus achieved the synergy of strength and ductility of the multiscale lamellar steel.<sup>[38]</sup> After that,

the value of  $n_i$  decreased with further strain. The decrease of  $n_i$  values is attributed to the saturated dislocation density is reached, the slip length and dislocation mobility are limited in ferrite grains.

It is interesting that the  $n_i$  of specimen annealed 10 and annealed 30 minutes are near each other. The strain hardening rate curves also support this finding, Figures 8(a) and (c). This observation is in correspondence with the fact that the specimen annealed 10 minutes occurs recovery and partially recrystallization due to short-time annealing (as shown in Figure 3(a), most large elongated ferrite grains), the dislocations generated after warm rolling are largely retained and the grain coarsening is not obvious, which means less freedom for the dislocations movement. Namely, specimen annealed 10 minutes have more saturated of the dislocations density compared with others, but the ability of multiplication dislocations is inferior to others and finally lead to the low-uniform elongation.

### C. Strengthening Mechanism

Multiple strengthening mechanisms can be used to predict the yield strength of steels with multiphase microstructure, according to the analysis of ultrafine or fine ( $\alpha + \theta$ ) structure,<sup>[16,37]</sup> the yield strength of multiscale lamellar ( $\alpha + \theta$ ) steel take into account the contribution of grain boundaries, cementite particles, forest dislocation and the role of frictional stress. This part will discuss the contributions course by these factors to the yield strength quantitatively. Therefore, the yield strength can simply be expressed as a linear manner:

$$\sigma_y = \sigma_0 + \sigma_g + \sigma_{SG} + \sigma_P + \sigma_d \quad [6]$$

where  $\sigma_y$  is the yield strength;  $\sigma_0$  is the sum of the frictional stress of ferrite grain and the solution strengthening and is approximately 118 MPa<sup>[16]</sup>;  $\sigma_g$  is the value of fine grain enhancement;  $\sigma_{SG}$  is the value of sub-grain strengthening;  $\sigma_P$  is the value of strengthening cause by cementite.  $\sigma_d$  is forest dislocation strengthening, the estimated value is 18 MPa at strain of 0.002 determined by Ray *et al.*<sup>[39]</sup>

Because of the multiscale lamellar nature, almost all specimens of low angle grain boundaries (sub-grain boundaries) and high angle grain boundaries are about half. Therefore, this part should be considered as the contribution of high angle grain boundary and sub-grain boundary to the strength, respectively. The contribution of grain boundary course by grain refinement to yield strength can be expressed using the Hall–Petch relationship as:

$$\sigma_g = K_y d^{-\frac{1}{2}} \quad [7]$$

where  $K_y$  is a proportional constant and is approximately 400 MPa $\cdot\mu\text{m}^{1/2}$  for high angle grain boundaries<sup>[37]</sup>; the value of  $d$  is shown in Table I. In terms of the contribution of sub-grain boundary to yield strength, the following formula could be used to calculate the strengthening of sub-grain boundary:

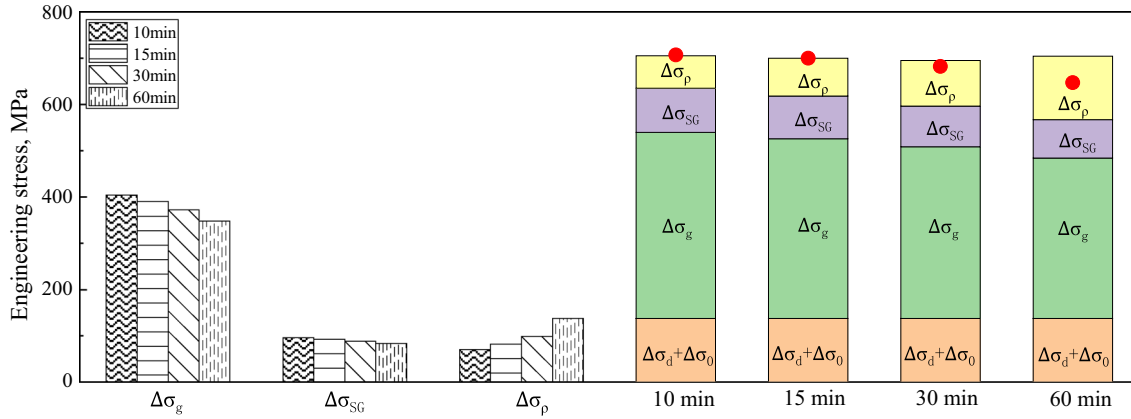


Fig. 10—Contribution of different strengthening mechanisms; the calculated value of the theoretical model is compared with the experimental value.

$$\sigma_{SG} = \alpha M G b \sqrt{\frac{1.5(S_v \theta)_{LAB}}{b}} \quad [8]$$

where  $\alpha$  is a constant and is about 0.24;  $M$  is the average Taylor coefficient and is about 2 for a volume centered cubic crystal;  $G$  is the shear modulus and the value of  $(\alpha + \theta)$  steel is about 81 GPa;  $b$  is the Burgers vector of the ferrite matrix and is 0.248;  $(S_v)_{LAB}$  is grain boundary surface area of sub-grain per unit volume,  $\approx \pi/2d_{SG}$ ;  $(\theta)_{LAB}$  is the mean orientation of low angle grain boundary.

The contribution of cementite particles to yield strength and GNDs around it can be estimated using the Orowan–Ashby relationship<sup>[40]</sup>:

$$\sigma_p = M \frac{0.84 G b}{2\pi(1 - \nu)^{0.5}(L - d_p)} \ln\left(\frac{d_p}{2b}\right) \quad [9]$$

where  $\nu$  is Poisson's ratio and is approximately 0.3;  $d_p$  is the average grain size of cementite;  $L$  is the average distance of cementite particles. Their values are shown in Table I.

Based on the discussion above, the contribution value of each individual mechanism to the yield strength of the specimen can be calculated respectively. To visualize the intensity contribution and the overall contribution of the four individual mechanisms, the bar chart in Figure 10 is summarized. It can be seen that there is little discrepancy between the theoretical calculation data (pile-up histogram) and the experimental value (marked with red dots), which further confirms the validity of the strengthening mechanisms mentioned above. The discrepancy (about 50 MPa) in specimen which annealed for 60 minutes may be attributed to below reason. The ferrite grains were developed during recrystallization process and the maximal one to 16  $\mu\text{m}$ , while the average grain size is 1.32  $\mu\text{m}$  due to multiscale distribution. It may affect our calculations of Hall–Petch relationship in some degree. As shown in Figure 10, with annealing time increasing, the contribution of grain refinement strengthening and sub-grain strengthening decreases,

while the contribution of cementite particles strengthening increased. The contribution of grain refinement strengthening is the main factor for all of the specimens.

## V. CONCLUSIONS

By optimizing the microstructure to improve the synergy of strength and ductility, the medium carbon steel with the initial pseudo-eutectoid structure was annealed at different times after warm rolling. The annealing stability of the dual-phase multiscale lamellar structure, the strengthening mechanisms and strain hardening ability of experimental steel were studied in depth.

1. The dual-phase multiscale distribution and lamellar structure characteristics are still retained after annealing. The structure has excellent stability when the annealing time is no longer than 30 minutes, while the proportion of high angle grain boundaries increased and the annealing stability of structure decreased when annealing for 60 minutes. In the multiscale lamellar structure, the ferrite in the original pearlite is more stable than the pro-eutectoid ferrite.
2. With the annealing time increasing, the strength of the studied steel decreased, while the elongation increased. Due to the high strain hardening capability, the multiscale lamellar  $(\alpha + \theta)$  steel annealing for 30 minutes demonstrated the best combination of strength and plasticity and the toughness was up to 5600 MPa pct. According to the modified C–J approach, the multiscale lamellar  $(\alpha + \theta)$  steel displayed a three-stage deformation behavior.
3. The contribution of different strengthening mechanisms to the yield strength of the experimental steel was investigated. The contribution of grain boundaries hardening is the dominant strengthening mechanism for the multiscale lamellar  $(\alpha + \theta)$  steel. As the annealing time increased, the contribution of grain boundaries decreased while the contribution of cementite particles increased.

## ACKNOWLEDGMENTS

The authors gratefully acknowledge financial supports from the National Natural Science Foundation of China (NSFC) (Grant Nos. 51974134); The Defense Industrial Technology Development Program (No. JCKY2018407C008); Natural Science Foundation of Hebei Province of China (No. E2017209237).

## REFERENCES

1. H.B. Li, L.F. Fan, L.S. Chen, and L.Y. Jia: *Ironmak. Steelmak.*, 2019, vol. 2019, pp. 1–7.
2. M. Jung, M. Kang, and Y.K. Lee: *Acta Mater.*, 2012, vol. 60, pp. 525–36.
3. S.G. Jansto: *Metall. Mater. Trans. B*, 2014, vol. 45B, pp. 438–44.
4. Q.T. Zhu, J. Li, J. Zhang, C.B. Shi, J.H. Li, and J. Huang: *Metall. Mater. Trans. B*, 2019, vol. 50B, pp. 1365–77.
5. K. Lu: *Acta Metall. Sin.* (in Chinese), 2015, vol. 51, pp. 1–10.
6. Y. Wang, M. Chen, F. Zhou, and E. Ma: *Nature*, 2002, vol. 419, pp. 912–15.
7. Z.S. You, L. Lu, and K. Lu: *Acta Mater.*, 2011, vol. 59, pp. 6927–37.
8. J.L. Ning, Y.T. Zhang, L. Huang, and Y.L. Feng: *Mater. Des.*, 2017, vol. 120, pp. 280–90.
9. M.H. Zhang, L.F. Li, J. Ding, Q.B. Wu, Y.D. Wang, J. Almer, F.M. Guo, and Y. Ren: *Acta Mater.*, 2017, vol. 141, pp. 294–303.
10. M.H. Zhang, Q. Tan, J. Ding, H.Y. Chen, F.M. Guo, Y. Ren, and Y.D. Wang: *Mater. Sci. Eng. A*, 2018, vol. 729, pp. 444–51.
11. S. Ahmad, L.F. Lv, L.M. Fu, H.R. Wang, W. Wang, and A.D. Shan: *Iron Steel Res. Int.*, 2019, vol. 32, pp. 361–71.
12. J.J. Sun, T. Jiang, Y.J. Wang, S.W. Guo, and Y.N. Liu: *Mater. Sci. Eng. A*, 2018, vol. 734, pp. 311–17.
13. W.L. Li, N.R. Tao, and K. Lu: *Scripta Mater.*, 2008, vol. 59, pp. 546–49.
14. P.F. Wang, Z. Han, and K. Lu: *Wear*, 2018, vol. 402, pp. 100–8.
15. J. Ning, B. Xu, M.S. Sun, C.Y. Zhao, Y.L. Feng, and W.P. Tong: *Mater. Sci. Eng. A*, 2018, vol. 735, pp. 275–87.
16. C.S. Zheng and L.F. Li: *Mater. Sci. Eng. A*, 2018, vol. 713, pp. 35–42.
17. X.L. Wu, M.X. Yang, F.P. Yuan, G.L. Wu, Y.J. Wei, X.X. Huang, and Y.T. Zhu: *Proc. Natl. Acad. Sci. USA.*, 2015, vol. 112, pp. 14501–05.
18. X.L. Wu and Y.T. Zhu: *Mater. Res. Lett.*, 2017, vol. 5, pp. 527–32.
19. L. Zhang, Z. Chen, Y.H. Wang, G.Q. Ma, T.L. Huang, G.L. Wu, and D.J. Jensen: *Scr. Mater.*, 2017, vol. 141, pp. 111–14.
20. J.J. Sun, T. Jiang, Y.J. Wang, S.W. Guo, and Y.N. Liu: *Mater. Sci. Eng. A*, 2020, vol. 785, p. 139339. <https://doi.org/10.1016/j.msea.2020.139339>.
21. M. Huang, G.H. Fan, L. Geng, G.J. Cao, Y. Du, H. Wu, T.T. Zhang, H.J. Kang, T.M. Wang, G.H. Du, and H.L. Xie: *Sci Rep*, 2016, vol. 6, pp. 1–10.
22. R. Song, D. Ponge, and D. Raabe: *Scripta Mater.*, 2005, vol. 52, pp. 1075–80.
23. L. Storojeva, D. Ponge, R. Kaspar, and D. Raabe: *Acta Mater.*, 2004, vol. 52, pp. 2209–20.
24. C. Prasad, P. Bhuyan, C. Kaithwas, R. Saha, and S. Mandal: *Mater. Des.*, 2018, vol. 139, pp. 324–35.
25. A. Ohmori, S. Torizuka, and K. Nagai: *ISIJ Int.*, 2004, vol. 44, pp. 1063–71.
26. R. Ding, Y.J. Yao, B.H. Sun, G. Liu, J.G. He, T. Li, X.H. Wan, Z.B. Dai, D. Ponge, D. Raabe, C. Zhang, A. Godfrey, G. Miyamoto, T. Furuhara, Z.G. Yang, S. van der Zwaag, and H. Chen: *Sci. Adv.*, 2020, vol. 6, p. 1430.
27. M. Jafari, C. Bang, J.C. Han, K. Kim, S. Na, C.G. Park, and B. Lee: *J. Mater. Sci. Technol.*, 2020, vol. 1, pp. 1–11.
28. X. Zhou, X.Y. Li, and K. Lu: *Science*, 2018, vol. 360, pp. 526–30.
29. X.L. Liang, H. Wang, Q.F. Pan, J.Y. Zheng, H.Q. Liu, R.Q. Zhang, Y. Xu, and Q.Y. Dan: *J. Iron Steel Res. Int.*, 2020, vol. 27, pp. 549–65.
30. J.H. Hollomon: *Trans. AIME*, 1945, vol. 162, pp. 223–49.
31. M.F. Ashby: *Philos. Mag.*, 1970, vol. 21, pp. 399–424.
32. Y. Estrin and H. Mecking: *Acta Metall.*, 1984, vol. 32, pp. 57–70.
33. C. Crussard and J. Mech: *Phys. Solids*, 1957, vol. 5, pp. 95–114.
34. S.A. Etesami and M.H. EnayatibAli: *Mater. Sci. Eng. A*, 2017, vol. 682, pp. 296–303.
35. H.W. Swift and J. Mech: *Phys. Solids*, 1952, vol. 1, pp. 1–18.
36. M.X. Yang, R.G. Li, P. Jiang, F.P. Yuan, Y.D. Wang, Y.T. Zhu, and X.L. Wu: *Mater. Res. Lett.*, 2019, vol. 7, pp. 433–38.
37. X.L. Wu, P. Jiang, L. Chen, J.F. Zhang, F.P. Yuan, and Y.T. Zhu: *Mater. Res. Lett.*, 2014, vol. 2, pp. 185–91.
38. C.S. Zheng, L.F. Li, and Y.D. Wang: *Mater. Sci. Eng. A*, 2015, vol. 631, pp. 181–88.
39. K.K. Ray and D. Mondal: *Acta Metall. Mater.*, 1991, vol. 39, pp. 2201–08.
40. C.S. Zheng, L.F. Li, W. Yang, W.Y. Yang, and Z.Q. Sun: *Mater. Sci. Eng. A*, 2014, vol. 617, pp. 31–8.

**Publisher's Note** Springer Nature remains neutral with regard to jurisdictional claims in published maps and institutional affiliations.